nature physics

ARTICLES

https://doi.org/10.1038/s41567-021-01321-0

Check for updates

Evidence for quantum spin liquid behaviour in single-layer 1T-$TaSe_2$ from scanning tunnelling microscopy

Wei Ruan[1,2,3,16], Yi Chen[1,2,16], Shujie Tang[4,5,6,7,8], Jinwoong Hwang[4,6,9], Hsin-Zon Tsai[1,10], Ryan L. Lee[2], Meng Wu[1,2], Hyejin Ryu[6,11], Salman Kahn[2], Franklin Liou[2], Caihong Jia[1,2,12], Andrew Aikawa[2], Choongyu Hwang[9], Feng Wang[1,2,13], Yongseong Choi[14], Steven G. Louie[1,2], Patrick A. Lee[15], Zhi-Xun Shen[4,5], Sung-Kwan Mo[6] and Michael F. Crommie[1,2,13] ✉

Two-dimensional triangular-lattice antiferromagnets are predicted under some conditions to exhibit a quantum spin liquid ground state with no energy barrier to create emergent, fractionalized spinon excitations that carry spin but no charge. Materials that realize this kind of spin liquid are expected to have a low-energy behaviour described by a spinon Fermi surface. Directly imaging the resulting spinons, however, is difficult due to their chargeless nature. Here we use scanning tunnelling spectroscopy to image density waves consistent with the predictions of spinon density modulation arising from a spinon Fermi surface instability in single-layer 1T-$TaSe_2$. We confirm the existence of a triangular lattice of localized spins in this material by contacting it with a metallic 1H-$TaSe_2$ substrate and measuring the Kondo effect. Spectroscopic imaging of isolated single-layer 1T-$TaSe_2$ reveals long-wavelength super-modulations at Hubbard band energies, consistent with the predicted behaviour of itinerant spinons. These super-modulations allow the direct experimental measurement of the spinon Fermi wavevector, in good agreement with theoretical predictions for a two-dimensional quantum spin liquid.

Since their first prediction by Anderson in 1973 (ref. [1]), quantum spin liquids (QSLs) have been intensely investigated[2–7] as candidates to host exotic quantum phenomena such as fractionalized elementary excitations[2–4], topological order[4,5] and unconventional superconductivity[6,7]. QSLs are a novel state of matter predicted to arise in quantum antiferromagnets where geometric frustration and quantum fluctuations are strong enough to prevent a magnetically ordered ground state[2–4]. A key to understanding the QSL state is its low-energy physics, often dominated by emergent fractional fermions (termed spinons) that carry spin-1/2 but no charge[2–4]. Many QSL models are based on two-dimensional (2D) triangular-lattice Mott insulators[2–4], and several material candidates incorporating coupled 2D layers have been found to exhibit behaviour consistent with spinon excitations[8–10]. It remains debatable whether the spinons in such systems are gapped or not[4,8–10], but increasing evidence[10] suggests the existence of gapless spinons that exhibit a Fermi surface[2–4,8–13].

Imaging the itinerant spinons, however, is challenging due to their fractional and chargeless nature. Some predictions suggest that the spinon Fermi surface should host instabilities leading to spinon spatial patterns[13] that can, in principle, be imaged by single-particle scanned probes[14]. Bulk 1T-TaS_2 has been suggested as one such QSL candidate[15–21]. This layered material is believed to exhibit a Mott-insulating ground state that cooperatively arises from a Star-of-David charge density wave (CDW)[22–24]. Each Star-of-David cluster contributes one localized spin, thus forming a triangular spin lattice. Some evidence for QSL behaviour in bulk 1T-TaS_2 has been found, such as the absence of magnetic order down to millikelvin temperature[17–19] and a linear term in the thermal conductivity[20,21], but QSL physics here is complicated by interlayer coupling. This is because interlayer coupling can lead to spin delocalization and/or interlayer spin-singlet formation, which are detrimental to the formation of a gapless QSL state[15,19,25–27].

Here we report experimental evidence supporting the existence of a QSL-based spinon Fermi surface in single-layer (SL) 1T-$TaSe_2$ through the use of scanning tunnelling microscopy/scanning tunelling spectroscopy (STM/STS). SL 1T-$TaSe_2$ is a newly discovered 2D Mott insulator that exhibits a low-temperature Star-of-David CDW

[1]Materials Sciences Division, Lawrence Berkeley National Laboratory, Berkeley, CA, USA. [2]Department of Physics, University of California, Berkeley, CA, USA. [3]Department of Physics, Fudan University, Shanghai, China. [4]Stanford Institute for Materials and Energy Sciences, SLAC National Accelerator Laboratory and Stanford University, Menlo Park, CA, USA. [5]Geballe Laboratory for Advanced Materials, Departments of Physics and Applied Physics, Stanford University, Stanford, CA, USA. [6]Advanced Light Source, Lawrence Berkeley National Laboratory, Berkeley, CA, USA. [7]CAS Center for Excellence in Superconducting Electronics, Shanghai Institute of Microsystem and Information Technology, Chinese Academy of Sciences, Shanghai, China. [8]School of Physical Science and Technology, Shanghai Tech University, Shanghai, China. [9]Department of Physics, Pusan National University, Busan, Korea. [10]International Collaborative Laboratory of 2D Materials for Optoelectronic Science and Technology of Ministry of Education, Engineering Technology Research Center for 2D Material Information Function Devices and Systems of Guangdong Province, Shenzhen University, Shenzhen, China. [11]Center for Spintronics, Korea Institute of Science and Technology, Seoul, Korea. [12]Henan Key Laboratory of Photovoltaic Materials, Center for Topological Functional Materials, Henan University, Kaifeng, China. [13]Kavli Energy NanoScience Institute at the University of California Berkeley and the Lawrence Berkeley National Laboratory, Berkeley, CA, USA. [14]Advanced Photon Source, Argonne National Laboratory, Argonne, IL, USA. [15]Department of Physics, Massachusetts Institute of Technology, Cambridge, MA, USA. [16]These authors contributed equally: Wei Ruan, Yi Chen. ✉e-mail: crommie@berkeley.edu

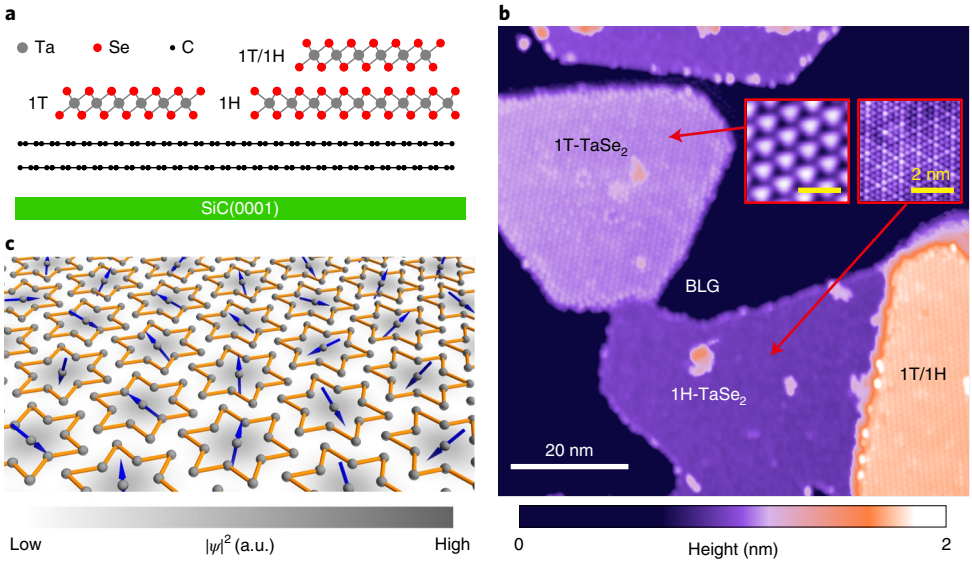

Fig. 1 | Structure of SL $TaSe_2$ and 1T/1H vertical heterostructures. a, Side view of the crystal structures of SL 1T-$TaSe_2$, 1H-$TaSe_2$ and 1T/1H vertical heterostructure on BLG-terminated SiC(0001). **b**, STM topographic image shows SL 1T-$TaSe_2$, SL 1H-$TaSe_2$ and 1T/1H vertical heterostructure on BLG/SiC(0001) (scanned at sample bias $V_b = -1$ V and tunnelling current $I_t = 5$ pA). The insets are close-up images of the SL 1T and 1H islands (scanned at $V_b = -0.5$ V, $I_t = 30$ pA and $V_b = 50$ mV, $I_t = 1.3$ nA, respectively) ($T = 5$ K). **c**, Schematic of the triangular spin lattice and Star-of-David CDW pattern in 1T-$TaSe_2$. Each star consists of 13 Ta atoms and has a localized spin represented by the blue arrow at the centre of the star. The squared wavefunction amplitude ($|\psi|^2$) of the localized electrons is represented by grey shading.

phase similar to bulk 1T-TaS_2 (that is, the Star-of-David cells are centred at the Ta atoms; Supplementary Fig. 1), but which does not suffer from the disadvantages of interlayer coupling between the 1T layers[28,29]. We report two experimental findings that support the presence of a QSL in SL 1T-$TaSe_2$. First, we demonstrate the existence of localized spins on a triangular lattice in SL 1T-$TaSe_2$ through the observation of Kondo resonance at the Fermi level (E_F) when SL 1T-$TaSe_2$ is placed in contact with metallic 1H-$TaSe_2$. Next, we show evidence for a QSL-based spinon Fermi surface subject to Fermi surface instability in isolated SL 1T-$TaSe_2$ through the observation of long-wavelength super-modulations in the electronic local density of states (LDOS) at the Hubbard band energies. Such wave patterns are unexpected in an insulator but naturally occur in the presence of a spinon Fermi surface. The ability to access fractional spinon behaviour via a single-particle probe (that is, STM) arises from the decomposition of the injected electrons into spinons (chargeless spin-1/2 fractional particles) and chargons (spinless charged fractional particles)[14,30]. By imaging spinon-induced LDOS super-modulations, we can directly determine the spinon Fermi wavevector (k_F), in good agreement with theoretical predictions[15,16] for a 2D QSL.

Kondo resonance in a 1T/1H-$TaSe_2$ vertical heterostructure

SL $TaSe_2$ films were grown on epitaxial bilayer graphene (BLG)-terminated 6H-SiC(0001) substrates and also on cleaved graphite surfaces via molecular beam epitaxy (MBE)[29,31]. A single $TaSe_2$ layer contains one Ta atomic layer sandwiched between a pair of Se atomic layers, with each Ta atom coordinated by six Se atoms (Fig. 1a). The Se cage forms an octahedron in the metastable 1T phase and a trigonal prism in the stable 1H phase. Coexisting 1T and 1H phases were grown via MBE in the SL limit under controlled growth conditions, as shown by our STM images (Fig. 1b). Atomically flat 1T and 1H SL islands can be easily distinguished (close-up images of both phases are shown in the insets of Fig. 1b), which exhibit a triangular $\sqrt{13} \times \sqrt{13}$ Star-of-David CDW pattern for the 1T phase[29] and a 3×3 CDW pattern for the 1H phase[31]. Vertical heterostructures composed of a single 1T layer on top of a single 1H layer (1T/1H) are observed to display the Star-of-David CDW pattern in the top layer and the 3×3 CDW in the bottom layer (Fig. 1b and Supplementary Fig. 2b).

We verified the electronic structure of different $TaSe_2$ phases by measuring STM differential conductance (dI/dV) (which reflects the surface electronic LDOS) as a function of the sample bias voltage (V_b). The dI/dV spectra acquired on metallic SL 1H-$TaSe_2$ islands show finite LDOS at E_F accompanied by a slight suppression due to CDW formation (green curves in Fig. 2a), consistent with previous measurements[31]. The dI/dV spectra acquired on insulating SL 1T-$TaSe_2$ islands on BLG/SiC, on the other hand, show a Mott gap (red curves in Fig. 2a), also consistent with previous measurements[29]. Here the LDOS peak near $V_b = -0.3$ V is identified as the lower Hubbard band (LHB) and the upper Hubbard band (UHB) corresponds to the peaks near $V_b = 0.2$ V (UHB_1) and $V_b = 0.6$ V (UHB_2) (these are split due to reduced screening in two dimensions[29]). The electronic structure of both SL 1T and 1H phases was also identified using angle-resolved photoemission spectroscopy (ARPES) (Supplementary Fig. 3b), confirming the coexistence of both phases.

The dI/dV spectra acquired on the 1T/1H vertical heterostructures are very different from either of the bare SL spectra at the Hubbard band energy scale. The heterostructure spectra reveal a pronounced zero-bias peak (ZBP), which is absent from SLs (blue curves in Fig. 2a) and cannot be explained by doping[32–35] or strain (Supplementary Note 2.1). The ZBP was found to persist in every Star-of-David cell (Supplementary Fig. 2). We identify the ZBP as Kondo resonance[36,37], which is expected to arise when a local spin (from the 1T layer) couples to itinerant electrons in a metal (from the 1H layer)[38] (the absence of Kondo resonance for SL 1T-$TaSe_2$ on BLG is due to BLG's low carrier density and poor coupling to the 1T layer (Supplementary Note 2.2)). To test the Kondo hypothesis, we examined the ZBP feature over the temperature range of $5 \leq T \leq 70$ K, as plotted in Fig. 2b. The ZBP gradually broadens with increased temperature by an amount that cannot be accounted for by pure thermal broadening, but is well fitted by a thermally

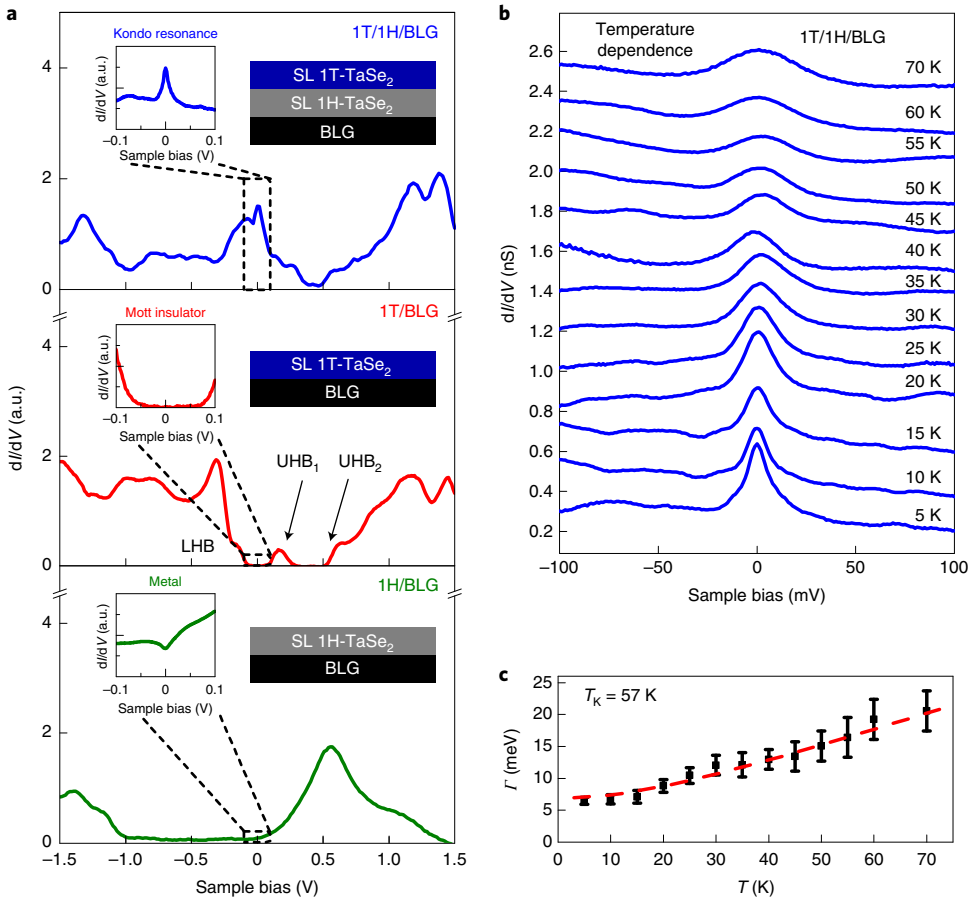

Fig. 2 | Kondo resonance observed in a 1T/1H-TaSe$_2$ vertical heterostructure. a, Local electronic structure measured at $T = 5$ K via dI/dV spectroscopy for SL 1H-TaSe$_2$ (green), SL 1T-TaSe$_2$ (red) and 1T/1H-TaSe$_2$ vertical heterostructure (blue) (1H: $V_b = -1.5$ V, $I_t = 30$ pA, $V_{mod} = 50$ mV; 1T: $V_b = 1.5$ V, $I_t = 40$ pA, $V_{mod} = 20$ mV; 1T/1H: $V_b = -1.5$ V, $I_t = 30$ pA, $V_{mod} = 20$ mV) (V_{mod} is the wiggle voltage of sample bias). The insets show higher-resolution dI/dV spectra (1H: $V_b = 0.1$ V, $I_t = 30$ pA, $V_{mod} = 5$ mV; 1T: $V_b = -0.25$ V, $I_t = 30$ pA, $V_{mod} = 2$ mV; 1T/1H: $V_b = -0.1$ V, $I_t = 30$ pA, $V_{mod} = 1$ mV) (the Kondo peak in the inset is sharper and taller compared with the lower-resolution measurement due to the use of a smaller wiggle voltage). **b**, Temperature dependence of the Kondo resonance peak observed in 1T/1H-TaSe$_2$ vertical heterostructures for $5 \leq T \leq 70$ K. The spectra are vertically offset for clarity ($V_b = -0.1$ V, $I_t = 30$ pA, $V_{mod} = 1$ mV). **c**, Temperature dependence of the intrinsic Kondo resonance width Γ (black with error bar). The error is estimated by the Γ threshold beyond which the fit significantly worsens[37]. The fit of equation (1) to the data (red dashed line) yields a Kondo temperature of $T_K = 57$ K.

convolved Fano line shape (Supplementary Note 2.3 and Supplementary Fig. 2d,e) with an intrinsic temperature-dependent width $\Gamma(T)$. The intrinsic resonance width as a function of temperature (T) is observed to follow the well-known Kondo expression[37]

$$\Gamma(T) = \sqrt{(\pi k_B T)^2 + 2(k_B T_K)^2}, \quad (1)$$

where k_B is the Boltzmann constant, yielding an estimated Kondo temperature of $T_K = 57 \pm 3$ K (red dashed line in Fig. 2c) and a resultant Kondo coupling of $J_K \approx 0.2$ eV (Supplementary Note 2.4). The observation of the Kondo resonance peak in every Star-of-David CDW cell suggests the existence of localized spins in isolated SL 1T-TaSe$_2$ that are arranged in a triangular lattice (Fig. 1c) (this behaviour is consistent with the typical lateral extension of Kondo peaks, which is of the order of 1 nm (ref. [39])), as well as with the coherence temperature of the 1T/1H Kondo lattice being lower than the STM base temperature of 5 K (Supplementary Note 2.4). Measuring the magnetism in SL materials via more direct methods is challenging. For example, we attempted to probe the magnetism in SL 1T-TaSe$_2$ using X-ray magnetic circular dichroism (XMCD), but this yielded no observable magnetization beyond the noise level (Supplementary Fig. 4).

Super-modulations in SL 1T-TaSe$_2$

We explored possible QSL behaviour in isolated SLs of 1T-TaSe$_2$ by characterizing long-wavelength super-modulations in the real-space electronic structure of this triangular spin lattice (here the 1T-TaSe$_2$ was supported by BLG/SiC rather than metallic 1H-TaSe$_2$ and so did not exhibit the Kondo effect (Supplementary Note 2.2)). Measurements were performed on SL 1T-TaSe$_2$ islands like the one shown in Fig. 3a, which exhibit dI/dV spectral characteristics of a Mott insulator (Fig. 3b). Figure 3c–g shows constant-height dI/dV maps acquired at different energies in the area outlined by a yellow dashed square in Fig. 3a, while Fig. 3h–l reveals the corresponding Fourier transform (FT) of each dI/dV map (Supplementary Fig. 5 shows the FT images without labels). The Star-of-David CDW pattern dominates the empty-state LDOS for energies above the UHB[29], as evident from the dI/dV map at $V_b = 1.0$ V (Fig. 3c) and its FT (Fig. 3h). Here the CDW triangular lattice yields six-fold symmetric FT peaks marked by red circles and labelled as the primary reciprocal lattice vectors $\mathbf{b}_i$ ($1 \leq i \leq 6$). These define the first Brillouin zone of the Star-of-David CDW (red hexagon). No other periodicities are seen at this energy.

New longer-wavelength super-modulations emerge at lower energies closer to the Hubbard band energies (that is, UHB$_2$, UHB$_1$ and LHB). At energies near UHB$_2$ ($V_b = 0.62$ V), for example, a new

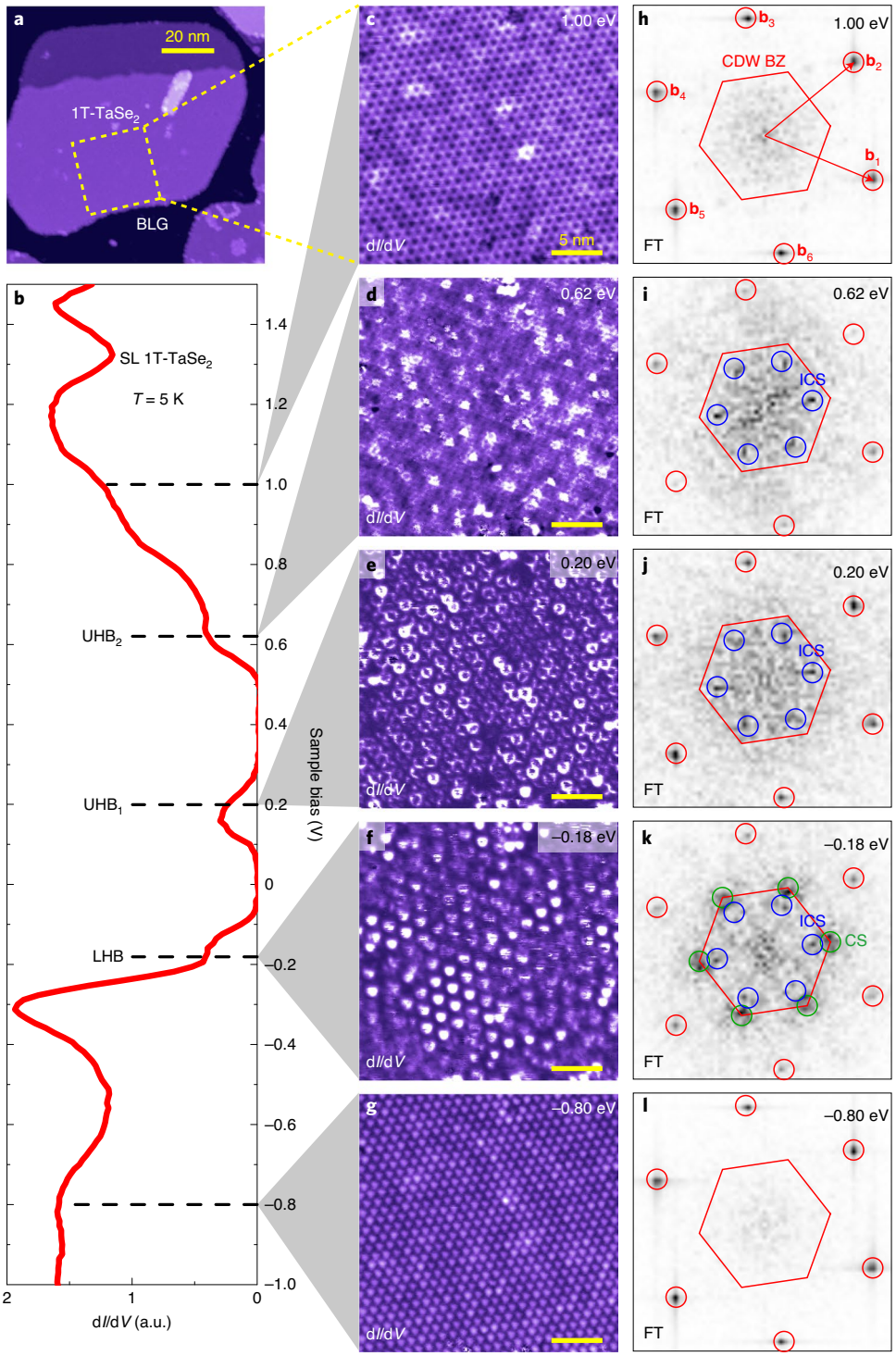

Fig. 3 | Super-modulations in SL 1T-$TaSe_2$ visualized by spectroscopic imaging. a, Large-scale topographic image of an SL 1T-$TaSe_2$ island ($V_b = -1$ V, $I_t = 2$ pA). **b**, The dI/dV spectrum of SL 1T-$TaSe_2$ ($V_b = 1.5$ V, $I_t = 40$ pA, $V_{mod} = 20$ mV). **c**–**g**, Constant-height dI/dV maps at energies of 1.00 eV (**c**), 0.62 eV (**d**), 0.20 eV (**e**), −0.18 eV (**f**) and −0.80 eV (**g**) acquired in the area indicated by the yellow dashed square in **a** ($I_t = 30$ pA, $V_{mod} = 20$ mV). **h**–**l**, Corresponding FTs of the dI/dV maps in **c**–**g**. FT peaks circled in red reflect the primary reciprocal lattice vectors of the Star-of-David CDW and the red hexagon represents the CDW Brillouin zone (BZ). FT peaks circled in blue (**i**–**k**) reflect incommensurate super-modulation (ICS) at 0.62, 0.20 and −0.18 V. FT peaks circled in green (**k**) reflect commensurate super-modulation (CS) ($T = 5$ K).

super-modulation is clearly seen in the real-space image of Fig. 3d as bright patches of enhanced LDOS (also see Supplementary Fig. 6d). This structure corresponds to a triangular grid rotated by 30° from the CDW lattice with an incommensurate lattice constant slightly larger than $\sqrt{3}a$ (Supplementary Fig. 6), where a is the CDW lattice constant. This incommensurate super-modulation (ICS) is distinctly shown in Fig. 3i (FT of the map shown in Fig. 3d), which shows new peaks marked by blue circles along

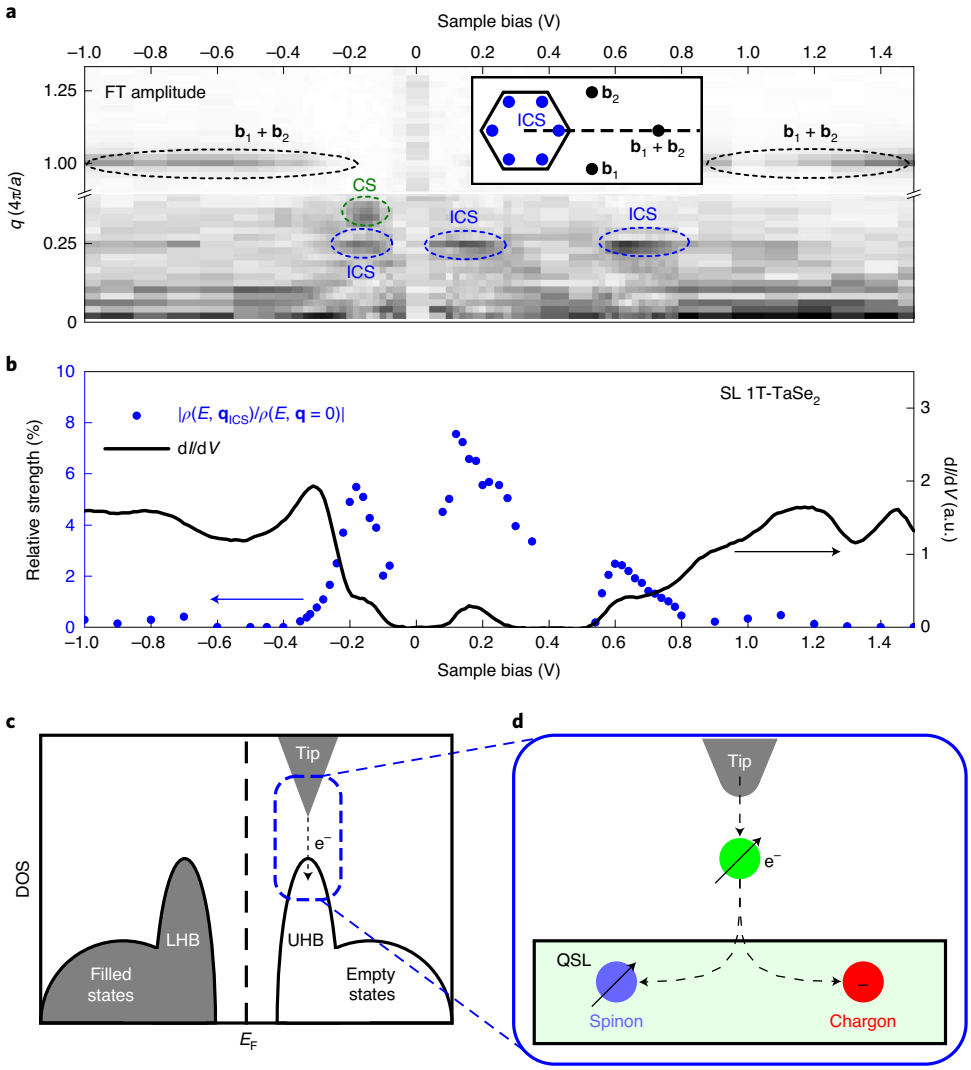

Fig. 4 | Energy dependence of super-modulations in SL 1T-TaSe$_2$. a, Plot of FT amplitude as a function of both wavevector $\mathbf{q} = q(\mathbf{b}_1 + \mathbf{b}_2)$ (q is measured in units of $|\mathbf{b}_1 + \mathbf{b}_2| = 4\pi/a$) along the Γ–K direction (y axis, indicated by the black dashed line in the inset) and sample bias voltage (x axis). High FT amplitude (dark colour) appears at $\mathbf{b}_1 + \mathbf{b}_2$ (black dashed ovals), ICS wavevector (blue dashed ovals) and CS wavevector (green dashed oval) ($T = 5$ K). **b**, Energy dependence of the ICS strength (blue dots) shows enhanced amplitude at Hubbard band energies. The ICS strength is defined as the FT amplitude at the ICS wavevector ($\rho(E, \mathbf{q}_{ICS})$) divided by the FT amplitude at $\mathbf{q} = 0$ ($\rho(E, \mathbf{q} = 0)$). The reference dI/dV spectrum is plotted in black ($T = 5$ K). **c**, Schematic of the density of states (DOS) of a Mott insulator. **d**, Sketch of a tip–QSL tunnel junction. An electron injected into the strongly correlated UHB of the QSL decays into a spinon and a chargon.

the Γ–K directions inside the CDW Brillouin zone. The ICS wavevector, $\mathbf{q}_{ICS}$, can be written in terms of the CDW reciprocal lattice vectors as $\mathbf{q}_{ICS} = q_{ICS}(\mathbf{b}_1 + \mathbf{b}_2)$, where $q_{ICS} = 0.241 \pm 0.009$ (q_{ICS} is obtained from the Gaussian fits of the FTs acquired on ten different islands with five different tips (Supplementary Fig. 7)).

The ICS pattern is also observed when energy is further lowered to UHB$_1$, as observed in the dI/dV map at $V_b = 0.2$ V (Fig. 3e) and the corresponding FT (Fig. 3j). The ICS is often obscured in real-space images due to mixing with the CDW pattern (Supplementary Note 1), but its FT peaks are easily resolved from the CDW wavevectors (Fig. 3j). The ICS persists as the energy is lowered to the LHB, as observed in the dI/dV map at $V_b = -0.18$ V (Fig. 3f), which yields FT peaks at $\mathbf{q}_{ICS}$ (Fig. 3k). The filled-state LHB measurement, however, differs from the empty-state UHB measurements in that it also exhibits short-range commensurate super-modulation (CS) of wavelength $\sqrt{3}a$ that yields broad FT peaks at the K points of the CDW Brillouin zone (green circles in Fig. 3k and Supplementary Fig. 8). Both ICS and CS disappear at energies below the LHB where only the Star-of-David CDW remains as shown by the dI/dV map at $V_b = -0.8$ V (Fig. 3g) and its corresponding FT (Fig. 3l).

The complete energy dependence of super-modulations over the energy range of $-1.0\,\text{V} < V_b < 1.5\,\text{V}$ is shown in Fig. 4a,b (Supplementary Figs. 9 and 10 show additional data at selected energies). Here the energy-dependent FT amplitude along the Γ–K direction (black dashed line in Fig. 4a, inset) as a function of wavevector $\mathbf{q} = q(\mathbf{b}_1 + \mathbf{b}_2)$ shows three main features: (1) the CDW reciprocal lattice vector $\mathbf{b}_1 + \mathbf{b}_2$ ($q = 1$) over a wide energy range (black dashed ovals), (2) CS ($q = 1/3$) in the filled-state LHB (green dashed oval) and (3) ICS ($q = q_{ICS} \approx 1/4$) in both LHB and UHB regimes (blue dashed ovals). We observe that the ICS wavevector is independent of energy, but its amplitude is not. To better visualize the energy dependence of the ICS amplitude, its strength is defined as the ICS FT peak amplitude $\rho(E, \mathbf{q}_{ICS})$ normalized by the FT peak amplitude $\rho(E, \mathbf{q} = 0)$ (equivalent to the spatially averaged surface LDOS). Figure 4b shows that this ratio, $|\rho(E, \mathbf{q}_{ICS})/\rho(E, \mathbf{q} = 0)|$ (blue dots), is small at all energies except for the LHB and UHB

regimes (the dI/dV spectrum of a single 1T-$TaSe_2$ layer is plotted for reference (black line)). The temperature dependence of the ICS amplitude (Supplementary Fig. 11) shows that it decreases as temperature increases and completely vanishes by $T = 77$ K, whereas the Star-of-David CDW remains even up to room temperature.

To investigate possible substrate effects on the behaviour of the observed super-modulation, SL 1T-$TaSe_2$ was also grown on cleaved highly oriented pyrolytic graphite (HOPG) via MBE and characterized by STM/STS. These samples also exhibit Star-of-David CDW order and Mott-insulating behaviour similar to films grown on BLG/SiC, as shown by the STM images and dI/dV spectra in Supplementary Fig. 12. STM images acquired in the LHB of SL 1T-$TaSe_2$/HOPG and their FTs show the same ICS pattern, as seen for SL 1T-$TaSe_2$/BLG/SiC (Supplementary Fig. 12d,e). However, an additional 2×2 super-modulation (with respect to the CDW lattice) is sometimes seen for SL 1T-$TaSe_2$/HOPG in the LHB that has FT peaks near the M points (Fig. 5d and Supplementary Fig. 12f–k) (this was observed in two out of 11 islands). We refer to this new super-modulation wavevector as $\mathbf{q}_M$. Also, $\mathbf{q}_{ICS}$ and $\mathbf{q}_M$ were never simultaneously observed on the same SL 1T-$TaSe_2$/HOPG island.

Relationship between super-modulations and QSL behaviour

Our experimental results support the hypothesis that SL 1T-$TaSe_2$ is a 2D QSL. The first piece of evidence is that SL 1T-$TaSe_2$ contains a triangular lattice of localized spins, an essential ingredient for a QSL. This evidence is provided by our observation of the Kondo effect in 1T layers supported by a 1H layer, which implies that each Star-of-David cell in isolated SL 1T-$TaSe_2$ contains a single quantum spin (such Kondo screening does not occur when 1T layers are supported by graphene (Supplementary Note 2.2)). The second piece of evidence is the long-wavelength super-modulations that we observe in SL 1T-$TaSe_2$ (when it is supported by graphene) via STS imaging. These periodicities lie at the precise energies and wavevectors expected for a QSL, as discussed below.

Before describing how these super-modulations are explained by QSL considerations, however, we first rule out possible alternative explanations. The first alternative possibility is electronic quasiparticle interference (QPI). Our observed ICS pattern is inconsistent with QPI because its wavelength is energy independent over the Hubbard bandwidths. There are also no notable electronic structure features at the Hubbard band edges that might induce a QPI signal at $\mathbf{q}_{ICS}$ (Supplementary Fig. 13). The second alternative possibility is structural distortion such as a moiré pattern and/or a surface reconstruction. This explanation is unlikely because the observed super-modulations exist only over very specific energy ranges involving the Hubbard bands, suggesting that they are electronic and/or spin-based phenomena. To further exclude moiré patterns involving complex BLG/SiC reconstructions, we point to the fact that SL 1T-$TaSe_2$/HOPG exhibits the same ICS modulation as SL 1T-$TaSe_2$/BLG/SiC (Supplementary Fig. 12). This is important because HOPG has no reconstruction and cannot combine with 1T-$TaSe_2$ to yield an ICS moiré pattern. We additionally see no evidence of the super-modulation in low-energy electron diffraction patterns[29], and no evidence that it is a strain effect (Supplementary Note 3.1). Reconstruction of the Star-of-David CDW (that is, subharmonic phonon softening) is also unlikely since the Star-of-David CDW is accounted for by ab initio calculations that show no ICS distortion[40], and the temperature dependences of ICS and CDW are very different (Supplementary Fig. 11). The last alternative possibility is Peierls-type or correlation-driven charge order. The former typically requires an electron Fermi surface, while the latter usually appears at much lower energy scales than the Hubbard bands[32]. Such behaviour is inconsistent with the ICS observed in our system and has no reasonable connection to the new periodicities seen here (that is, $\mathbf{q}_{ICS}$ and $\mathbf{q}_M$).

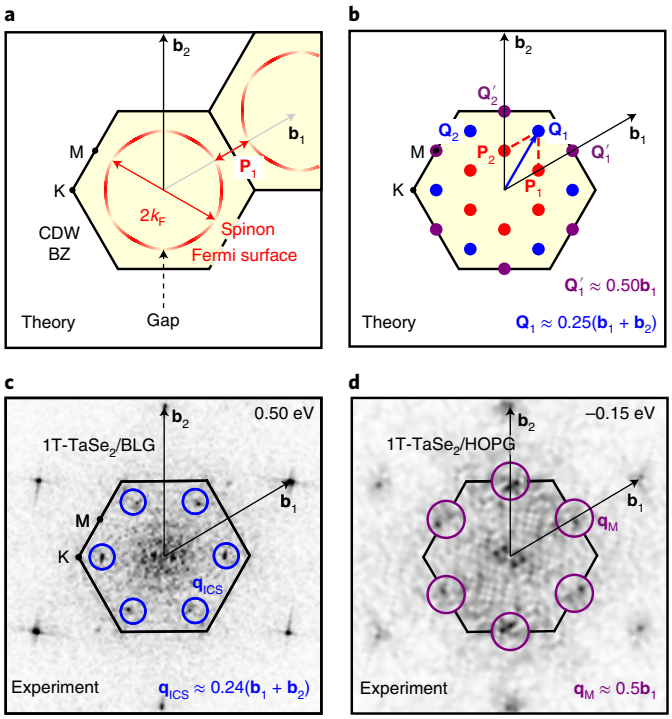

Fig. 5 | Super-modulation periodicities predicted from the spinon Fermi surface compared with experiment. a, Schematic of the spinon Fermi surface at half filling (red) with partial gaps opening along the Γ–M directions. The black hexagon is the Star-of-David CDW Brillouin zone and the black arrows ($\mathbf{b}_i$) are the primary reciprocal lattice vectors of the CDW Brillouin zone ($1 \le i \le 6$, only $\mathbf{b}_1$ and $\mathbf{b}_2$ are labelled). The spinon Fermi surface instability wavevectors $\mathbf{P}_i$ (red arrow) connect the partial gaps on different spinon Fermi surfaces in an extended zone scheme. **b**, Spinon Fermi surface instability wavevectors $\mathbf{P}_i$ (red dots) and harmonics $\mathbf{Q}_i$ (blue dots) and $\mathbf{Q}_i'$ (purple dots) in the CDW Brillouin zone. **c**, FT of the STM image of 1T-$TaSe_2$/BLG at $V_b = 0.5$ V (STM image shown in Supplementary Fig. 7a, inset). Experimental ICS wavevectors $\mathbf{q}_{ICS}$ are circled in blue ($T = 5$ K). **d**, FT of the STM image of 1T-$TaSe_2$/HOPG at $V_b = -0.15$ V (STM image shown in Supplementary Fig. 12j). Experimental super-modulation wavevectors $\mathbf{q}_M$ close to the M points are circled in purple ($T = 5$ K).

The presence of a QSL-based spinon Fermi surface, on the other hand, very naturally explains both energy dependence and wavevectors of the $\mathbf{q}_{ICS}$ and $\mathbf{q}_M$ super-modulations observed in a single 1T-$TaSe_2$ layer. The starting point here is that our system hosts a QSL state with a half-filled spinon band. This idea is supported by density matrix renormalization group calculations based on the triangular-lattice t–J model with a ring exchange term that simulates the Hubbard model near a Mott transition[16]. In these calculations, the spin-correlation peaks in the Γ–M directions are missing[16], which suggests that a partial gap opens at the spinon Fermi wavevector k_F along the Γ–M directions due to a Fermi surface instability (the calculations, however, do not reveal the precise source of the instability (Fig. 5a)). The value of the predicted spinon k_F comes from the spinon band structure, which is modelled using a zero-flux mean-field tight-binding Hamiltonian[10] with nearest-neighbour spinon hopping. This yields a value of the spinon Fermi wavevector in the Γ–M direction of $k_F \approx 0.375$ reciprocal lattice units (r.l.u.) (inclusion of next-nearest-neighbour hopping does not notably alter k_F; Supplementary Note 3.2 and Supplementary Fig. 14).

The predicted instability of the spinon Fermi surface implies the existence of primary order wavevectors $\mathbf{P}_i = (1 - 2k_F)\mathbf{b}_i \approx 0.249\mathbf{b}_i$ that couple the gapped spinon Fermi surface regions in an extended

zone scheme, as shown in Fig. 5 (red arrows (Fig. 5a) and red dots (Fig. 5b)). The absence of experimental LDOS super-modulations at these predicted wavevectors (Fig. 5c,d), however, suggests that the spinon Fermi surface instability is not a spinon density wave. Other candidates for the spinon Fermi surface instability, such as a spinon pair density wave[13,41–43] or a spinon spin density wave, are more consistent with our experiment since they cannot be directly imaged by conventional STM because they reflect spatial modulations in either the spinon pair channel (in the case of spinon pair density wave) or the pure spin channel (in the case of spinon spin density wave). However, a composite spinon density wave that is observable by conventional STM can be induced at higher harmonics of the primary $\mathbf{P}_i$ vectors. This can be rationalized in a straightforward manner from either a scattering picture or a Landau formulation[44,45] (Supplementary Notes 3.3 and 3.4 and Supplementary Fig. 15).

We find that although the primary $\mathbf{P}_i$ vectors do not coincide with our observed super-modulation wavevectors, their higher harmonics (labelled $\mathbf{Q}_i$ and $\mathbf{Q}'_i$ in Fig. 5b) match our experimental super-modulations quite well. For example, the theoretical harmonics $\mathbf{Q}_i = \mathbf{P}_i + \mathbf{P}_{i+1} \approx 0.249(\mathbf{b}_i + \mathbf{b}_{i+1})$ match our experimentally measured super-modulations at $\mathbf{q}_{\mathrm{ICS}} = (0.241 \pm 0.009)(\mathbf{b}_i + \mathbf{b}_{i+1})$ (Fig. 5c), while the theoretical harmonics $\mathbf{Q}'_i = 2\mathbf{P}_i$ match our experimentally measured super-modulations at $\mathbf{q}_{\mathrm{M}}$ (Fig. 5d). Our experimental observation of the predicted harmonics at both $\mathbf{Q}_i$ and $\mathbf{Q}'_i$ strongly suggests the existence of a hidden primary wavevector $\mathbf{P}_i$ and points to a spinon Fermi surface subject to instability at $\mathbf{P}_i$ in SL 1T-$TaSe_2$.

If we work backwards and compare our measured value of $\mathbf{q}_{\mathrm{ICS}} = q_{\mathrm{ICS}}(\mathbf{b}_1 + \mathbf{b}_2)$ to the theoretically predicted composite spinon density wavevectors $\mathbf{Q}_i = \mathbf{P}_i + \mathbf{P}_{i+1}$ using $\mathbf{P}_i = (1 - 2k_{\mathrm{F}})\mathbf{b}_i$, then we find that the spinon Fermi wavevector can be written as $k_{\mathrm{F}} = (1 - q_{\mathrm{ICS}})/2$. This leads to an experimental value of $k_{\mathrm{F}} = 0.380 \pm 0.005$ r.l.u., in good agreement with the theoretically predicted value of $k_{\mathrm{F}} = 0.375$ r.l.u. This value of k_{F} is also consistent with our ARPES data that show enhanced intensity centred at Γ, which greatly weakens for in-plane momenta beyond k_{F} (Supplementary Fig. 3). Our observed temperature dependence of the ICS feature is also consistent with this physical picture since it suggests a spinon Fermi surface instability transition at a temperature of $T \approx 60$ K (Supplementary Fig. 11).

While the periodicities of our experimental super-modulations are well explained by the QSL-based spinon scenario described above, a remaining question is how an STM that works by injecting charged particles (that is, electrons) into a material can observe particles that have no charge (that is, spinons). The answer lies in the process of fractionalization, whereby strongly correlated electrons in a QSL are predicted to separate into spinons (which have spin and no charge) and chargons (which have charge and no spin). Due to constraints in the total occupation of spinons and chargons, modulation of the spinon density can induce a small density modulation in the physical charge[14]. However, an even stronger effect occurs in the tunnelling process since an electron injected into the QSL UHB (or removed from the LHB) will fractionalize into (or recombine from) a spinon and a chargon (schematic shown in Fig. 4c,d). The tunnelling probability thus depends on both spinon wave function and chargon wave function, and therefore, the tunnelling rate of an electron at a particular energy can be expressed as a convolution of spinons and chargons that sum to the right energy, as done previously to interpret the ARPES data[30,46] (Supplementary Note 3.5). Spatially periodic spinon density due to modulations from a spinon Fermi surface instability should thus modulate the quasiparticle tunnel rates at the Hubbard band energies[11–13,16] (Supplementary Note 3.5 and Supplementary Fig. 16). Our experimental observation of long-wavelength super-modulations confined to Hubbard band energies (Fig. 4a,b) supports this proposed mechanism whether the super-modulations are thought to arise from a composite order picture or from the scattering of spinons (both of which are essentially equivalent as described in Supplementary Notes 3.3 and 3.4).

Despite the agreement of our experimental results with the existence of a QSL spinon Fermi surface, some mysteries remain. For instance, the $\mathbf{P}_i$ vectors are also second-harmonic wavevectors of themselves (Supplementary Fig. 15b), and therefore, their absence in our experiment must be explained. One possible explanation is that this is a consequence of small structure factors at $\mathbf{P}_i$ (Supplementary Note 3.3). We note that the selective visibility of composite density waves at higher harmonics has also been observed in other materials[47] and might be affected by detailed defect and domain structures (Supplementary Fig. 12). Another open question is the origin of the experimental CS pattern at the K-point wavevectors. The CS pattern cannot be explained as a consequence of a spinon Fermi surface since K is not a harmonic of the $\mathbf{P}_i$ wavevectors. One possible explanation of the short-range CS is that our QSL phase is close to an antiferromagnetic ordered phase in the phase diagram, thus causing the CS to arise from short-range antiferromagnetic[48] fluctuations that are expected to be commensurate with the K points (Supplementary Note 4).

In conclusion, our STM measurements provide evidence that SL 1T-$TaSe_2$ is a QSL with a spinon Fermi surface. Our observation of the Kondo effect in 1T-$TaSe_2$/1H-$TaSe_2$ heterostructures implies that SL 1T-$TaSe_2$ exhibits a triangular spin lattice, and our STS maps of 1T-$TaSe_2$ super-modulations directly reveal the effects of a spinon Fermi surface instability in this material. Our experimentally determined value of the spinon Fermi wavevector, namely, $k_{\mathrm{F}} = 0.380 \pm 0.005$ r.l.u., closely matches the theoretically predicted value of $k_{\mathrm{F}} = 0.375$ r.l.u and supports the existence of a gapless QSL ground state. A single 1T-$TaSe_2$ layer thus provides a new platform to further investigate QSL phenomena such as the response of 2D QSLs to magnetic scatterers[14,49,50] and electrostatic doping[6,7,43].

Online content

Any methods, additional references, Nature Research reporting summaries, source data, extended data, supplementary information, acknowledgements, peer review information; details of author contributions and competing interests; and statements of data and code availability are available at https://doi.org/10.1038/s41567-021-01321-0.

Received: 28 September 2020; Accepted: 7 July 2021;
Published online: 19 August 2021

References

1. Anderson, P. W. Resonating valence bonds: a new kind of insulator? *Mater. Res. Bull.* **8**, 153–160 (1973).
2. Lee, P. A. An end to the drought of quantum spin liquids. *Science* **321**, 1306–1307 (2008).
3. Balents, L. Spin liquids in frustrated magnets. *Nature* **464**, 199–208 (2010).
4. Zhou, Y., Kanoda, K. & Ng, T.-K. Quantum spin liquid states. *Rev. Mod. Phys.* **89**, 025003 (2017).
5. Wen, X.-G. Quantum orders and symmetric spin liquids. *Phys. Rev. B* **65**, 165113 (2002).
6. Anderson, P. W. The resonating valence bond state in La_2CuO_4 and superconductivity. *Science* **235**, 1196–1198 (1987).
7. Lee, P. A. From high temperature superconductivity to quantum spin liquid: progress in strong correlation physics. *Rep. Prog. Phys.* **71**, 012501 (2008).
8. Shimizu, Y., Miyagawa, K., Kanoda, K., Maesato, M. & Saito, G. Spin liquid state in an organic Mott insulator with a triangular lattice. *Phys. Rev. Lett.* **91**, 107001 (2003).
9. Yamashita, M. et al. Highly mobile gapless excitations in a two-dimensional candidate quantum spin liquid. *Science* **328**, 1246–1248 (2010).
10. Shen, Y. et al. Evidence for a spinon Fermi surface in a triangular-lattice quantum-spin-liquid candidate. *Nature* **540**, 559–562 (2016).
11. Motrunich, O. I. Variational study of triangular lattice spin-1/2 model with ring exchanges and spin liquid state in κ-$(ET)_2Cu_2(CN)_3$. *Phys. Rev. B* **72**, 045105 (2005).
12. Lee, S. S. & Lee, P. A. U(1) gauge theory of the Hubbard model: spin liquid states and possible application to κ-$(BEDT\text{-}TTF)_2Cu_2(CN)_3$. *Phys. Rev. Lett.* **95**, 036403 (2005).

13. Lee, S. S., Lee, P. A. & Senthil, T. Amperean pairing instability in the U(1) spin liquid state with Fermi surface and application to κ-(BEDT-TTF)$_2$Cu$_2$(CN)$_3$. *Phys. Rev. Lett.* **98**, 067006 (2007).
14. Mross, D. F. & Senthil, T. Charge Friedel oscillations in a Mott insulator. *Phys. Rev. B* **84**, 041102(R) (2011).
15. Law, K. T. & Lee, P. A. 1T-TaS$_2$ as a quantum spin liquid. *Proc. Natl Acad. Sci. USA* **114**, 6996–7000 (2017).
16. He, W. Y., Xu, X. Y., Chen, G., Law, K. T. & Lee, P. A. Spinon Fermi surface in a cluster Mott insulator model on a triangular lattice and possible application to 1T-TaS$_2$. *Phys. Rev. Lett.* **121**, 046401 (2018).
17. Klanjšek, M. et al. A high-temperature quantum spin liquid with polaron spins. *Nat. Phys.* **13**, 1130–1134 (2017).
18. Kratochvilova, M. et al. The low-temperature highly correlated quantum phase in the charge-density-wave 1T-TaS$_2$ compound. *npj Quantum Mater.* **2**, 42 (2017).
19. Ribak, A. et al. Gapless excitations in the ground state of 1T-TaS$_2$. *Phys. Rev. B* **96**, 195131 (2017).
20. Yu, Y. J. et al. Heat transport study of the spin liquid candidate 1T-TaS$_2$. *Phys. Rev. B* **96**, 081111(R) (2017).
21. Murayama, H. et al. Effect of quenched disorder on the quantum spin liquid state of the triangular-lattice antiferromagnet 1T-TaS$_2$. *Phys. Rev. Res.* **2**, 013099 (2020).
22. Wilson, J. A., Di Salvo, F. J. & Mahajan, S. Charge-density waves and superlattices in the metallic layered transition metal dichalcogenides. *Adv. Phys.* **24**, 117–201 (1975).
23. Fazekas, P. & Tosatti, E. Electrical, structural and magnetic properties of pure and doped 1T-TaS$_2$. *Phil. Mag. B* **39**, 229–244 (1979).
24. Qiao, S. et al. Mottness collapse in 1T-TaS$_{2-x}$Se$_x$ transition-metal dichalcogenide: an interplay between localized and itinerant orbitals. *Phys. Rev. X* **7**, 041054 (2017).
25. Ritschel, T. et al. Orbital textures and charge density waves in transition metal dichalcogenides. *Nat. Phys.* **11**, 328–331 (2015).
26. Ma, L. et al. A metallic mosaic phase and the origin of Mott-insulating state in 1T-TaS$_2$. *Nat. Commun.* **7**, 10956 (2016).
27. Cho, D. et al. Nanoscale manipulation of the Mott insulating state coupled to charge order in 1T-TaS$_2$. *Nat. Commun.* **7**, 10453 (2016).
28. Nakata, Y. et al. Selective fabrication of Mott-insulating and metallic monolayer TaSe$_2$. *ACS Appl. Nano Mater.* **1**, 1456–1460 (2018).
29. Chen, Y. et al. Strong correlations and orbital texture in single-layer 1T-TaSe$_2$. *Nat. Phys.* **16**, 218–224 (2020).
30. Kim, B. J. et al. Distinct spinon and holon dispersions in photoemission spectral functions from one-dimensional SrCuO$_2$. *Nat. Phys.* **2**, 397–401 (2006).
31. Ryu, H. et al. Persistent charge-density-wave order in single-layer TaSe$_2$. *Nano Lett.* **18**, 689–694 (2018).
32. Cai, P. et al. Visualizing the evolution from the Mott insulator to a charge-ordered insulator in lightly doped cuprates. *Nat. Phys.* **12**, 1047–1051 (2016).
33. Ruan, W. et al. Relationship between the parent charge transfer gap and maximum transition temperature in cuprates. *Sci. Bull.* **61**, 1826–1832 (2016).
34. Battisti, I. et al. Universality of pseudogap and emergent order in lightly doped Mott insulators. *Nat. Phys.* **13**, 21–25 (2017).
35. Ruan, W. et al. Visualization of the periodic modulation of Cooper pairing in a cuprate superconductor. *Nat. Phys.* **14**, 1178–1182 (2018).
36. Hewson, A. C. *The Kondo Problem to Heavy Fermions* (Cambridge Univ. Press, 1993).
37. Nagaoka, K., Jamneala, T., Grobis, M. & Crommie, M. F. Temperature dependence of a single Kondo impurity. *Phys. Rev. Lett.* **88**, 077205 (2002).
38. Helmes, R. W., Costi, T. A. & Rosch, A. Kondo proximity effect: how does a metal penetrate into a Mott insulator? *Phys. Rev. Lett.* **101**, 066802 (2008).
39. Madhavan, V. V., Chen, W., Jamneala, T., Crommie, M. F. & Wingreen, N. S. Tunneling into a single magnetic atom: spectroscopic evidence of the Kondo resonance. *Science* **280**, 567–569 (1998).
40. Ge, Y. & Liu, A. Y. First-principles investigation of the charge-density-wave instability in 1T-TaSe$_2$. *Phys. Rev. B* **82**, 155133 (2010).
41. Galitski, V. & Kim, Y. B. Spin-triplet pairing instability of the spinon Fermi surface in a U(1) spin liquid. *Phys. Rev. Lett.* **99**, 266403 (2007).
42. Grover, T., Trivedi, N., Senthil, T. & Lee, P. A. Weak Mott insulators on the triangular lattice: possibility of a gapless nematic quantum spin liquid. *Phys. Rev. B* **81**, 245121 (2010).
43. Xu, X. Y., Law, K. T. & Lee, P. A. Pair density wave in the doped t–J model with ring exchange on a triangular lattice. *Phys. Rev. Lett.* **122**, 167001 (2019).
44. Agterberg, D. F. & Tsunetsugu, H. Dislocations and vortices in pair-density-wave superconductors. *Nat. Phys.* **4**, 639–642 (2008).
45. Fradkin, E., Kivelson, S. A. & Tranquada, J. M. Colloquium: theory of intertwined orders in high temperature superconductors. *Rev. Mod. Phys.* **87**, 457–482 (2015).
46. Tang, E., Fisher, M. P. A. & Lee, P. A. Low-energy behavior of spin-liquid electron spectral functions. *Phys. Rev. B* **87**, 045119 (2013).
47. Edkins, S. D. et al. Magnetic field–induced pair density wave state in the cuprate vortex halo. *Science* **364**, 976–980 (2019).
48. Huse, D. A. & Elser, V. V. Simple variational wave functions for two-dimensional Heisenberg spin-1/2 antiferromagnets. *Phys. Rev. Lett.* **60**, 2531–2534 (1988).
49. Ribeiro, P. & Lee, P. A. Magnetic impurity in a U(1) spin liquid with a spinon Fermi surface. *Phys. Rev. B* **83**, 235119 (2011).
50. Norman, M. R. & Micklitz, T. How to measure a spinon Fermi surface. *Phys. Rev. Lett.* **102**, 067204 (2009).

Methods

Sample growth and ARPES measurements. Both sample growth and ARPES measurements were performed at the HERS endstation of Beamline 10.0.1, Advanced Light Source, Lawrence Berkeley National Laboratory. SL $TaSe_2$ films were grown on both BLG/6H-SiC(001) and HOPG substrates in an ultrahigh-vacuum (UHV) MBE chamber under similar growth conditions as described elsewhere[29]. The substrate temperature was set at 660 °C, much higher than that for the growth of pure 1H-$TaSe_2$, to allow the simultaneous growth of SL 1T-$TaSe_2$ and SL 1H-$TaSe_2$, as well as vertical heterostructures composed of a 1T layer on top of a 1H layer. After growth, the samples were transferred in situ into the analysis chamber with a base pressure of 3×10^{-11} torr for ARPES measurements at 12 K. The photon energy was set at 50 eV with energy and angular resolution of 12 meV and 0.1°, respectively. The samples were then capped by Se capping layers with ~10 nm thickness for protection during transport through air to the UHV STM chamber.

STM/STS measurements. STM and STS measurements were performed in a low-temperature UHV STM system (CreaTec) at $T=5$ K (unless specified otherwise). Before the measurements, the samples were annealed in UHV at ~200 °C for 3 h to remove the Se capping layers and then immediately transferred in situ into the STM stage sitting at $T=5$ K. Electrochemically etched tungsten tips were calibrated on a Au(111) surface before measurements. The dI/dV spectra were collected using standard lock-in techniques (frequency $f=401$ Hz). Also, dI/dV mapping was performed in the constant-height mode (that is, with an open feedback loop).

XMCD measurements. XMCD measurements were performed at Beamline 4-ID-D, Advanced Photon Source, Argonne National Laboratory. Hard X-rays were used to probe the L_2 and L_3 edges of Ta at grazing incident angles to optimize the signal from SL 1T-$TaSe_2$ relative to the background noise from the substrate. The absorption spectra were collected in the fluorescence yield mode. SL 1T-$TaSe_2$/BLG samples were capped with Se layers during transport to the XMCD measurement chambers. The samples were mounted with the sample plane in the vertical direction. The X-ray beam size was adjusted to be 0.1 mm along the horizontal direction and 0.3 mm along the vertical direction.

Data availability

Source data are provided with this paper. All other data that support the findings of this study are available from the corresponding author upon reasonable request.

Code availability

The codes used in this study are available from the corresponding author upon reasonable request.

Acknowledgements

We thank D.-H. Lee, J. E. Moore and M. Zaletel for helpful discussions. This research was supported by the vdW Heterostructure program (KCWF16) (STM/STS measurements) and the Advanced Light Source (sample growth and ARPES measurements) funded by the Director, Office of Science, Office of Basic Energy Sciences, Materials Sciences and Engineering Division, US Department of Energy (DOE), under contract no. DE-AC02-05CH11231. Support was also provided by the National Science Foundation (NSF) via award no. DMR-1807233 (surface treatment and topographic characterization) and award no. DMR-1926004 (theoretical QPI analysis). Computational resources were provided by the NSF through the Extreme Science and Engineering Discovery Environment (XSEDE) resources. The work at the Stanford Institute for Materials and Energy Sciences and Stanford University (ARPES measurements) was supported by the Office of Basic Energy Sciences, Materials Sciences and Engineering Division, DOE. The work at Beamline 4-ID-D of the Advanced Photon Source, Argonne National Laboratory (X-ray absorption measurements), was supported by the Office of Science, Office of Basic Energy Sciences, DOE, under contract no. DE-AC02-06CH11357. P.A.L. acknowledges support by DOE Basic Energy Science award no. DE-FG02-03ER46076 (theoretical QSL analysis). S.T. acknowledges support by CPSF-CAS Joint Foundation for Excellent Postdoctoral Fellows. J.H. and C.H. acknowledge fellowship support from the NRF grant funded by the Korean government (MSIT) (no. 2021R1A2C1004266). H.-Z.T. acknowledges fellowship support from the Shenzhen Peacock Plan (grant nos. 827-000113, KQJSCX20170727100802505 and KQTD2016053112042971).

Author contributions

W.R., Y. Chen, P.A.L. and M.F.C. initiated and conceived this project. W.R., Y. Chen, R.L.L., H.-Z.T., S.K., F.L., C.J. and A.A. carried out the STM/STS measurements under the supervision of M.F.C. W.R., Y. Chen, F.W., P.A.L. and M.F.C. contributed to the microscopy data analysis. S.T., J.H. and H.R. performed the sample growth and ARPES measurements/analysis under the supervision of C.H., Z.-X.S. and S.-K.M. W.R., Y. Chen, R.L.L. and S.K. performed the XMCD measurements with support from Y. Choi. M.W. performed the DFT+U calculations under the supervision of S.G.L. P.A.L. provided theoretical support. W.R., Y. Chen and M.F.C. wrote the manuscript with the help from all the authors. All the authors contributed to the scientific discussion.

Competing interests

The authors declare no competing interests.

Additional information

Supplementary information The online version contains supplementary material available at https://doi.org/10.1038/s41567-021-01321-0.

Correspondence and requests for materials should be addressed to M.F.C.

Peer review information *Nature Physics* thanks the anonymous reviewer(s) for their contribution to the peer review of this work.

Reprints and permissions information is available at www.nature.com/reprints.